https://doi.org/10.1016/j.ijheatmasstransfer.2022.122969

Experimental and numerical study of heat transfer performance of a channel flow with an inverted flag

X.L. Zhong[a], S.C. Fu[a,*], K.C. Chan[a], L.Q. Wang[a], Christopher Y.H. Chao[b]

[a]Department of Mechanical Engineering, The University of Hong Kong, Hong Kong, China

[b]Department of Building Environment and Energy Engineering and Department of Mechanical Engineering, The Hong Kong Polytechnic University, Hong Kong

* Corresponding Author Tel.: +(852) 39102154

E-mail address: scfu@hku.hk

Address: Department of Mechanical Engineering, The University of Hong Kong, Hong Kong, China

Abstract

It has been demonstrated that flexible vortex generators, e.g., flapping flag, can significantly enhance heat transfer inside a heat sink. However, their heat transfer enhancement is only effective when they exhibit flapping behaviors, which require a flow velocity higher than the heat sink working velocity, and thus restraint their application. Minimizing the critical flapping velocity of the flags without sacrificing the heat transfer performance is needed. In this work, we study the cases of inverted flags with different thicknesses in a channel flow. Three flag motion modes are identified by a high-speed camera with increasing flow velocity. In the first mode transition, i.e., the flag starts flapping, the heat dissipation has the highest enhancement. Numerical simulation reveals that compared to the other motion modes, the flapping mode has the strongest average vorticity along the channel wall, leading to the highest heat dissipation among all flag motion modes. Experimental results show that the critical velocity can be as low as 1.5 m/s, at which the heat dissipation enhancement can be as high as 100%. The findings in this work significantly benefit the application of flexible vortex generators in heat sinks, by enabling a decrease in critical velocity and a good enhancement in heat dissipation.

Keywords

Flexible vortex generators, Convective heat transfer, Fluid-structure interaction, Inverted flag, Flag mode, Vorticity.

Nomenclature

A_{total}	Total heat transfer area, m^2
D	Channel width, m
E	Young's modulus, Pa
f	Friction factor
h	Average heat transfer coefficient, $W\ m^{-2}\ K^{-1}$

H	Channel width of the test section in simulation, m
k	Air thermal conductivity, W m^{-1} K^{-1}
L	Channel length of the test section in simulation, m
Nu	Nusselt number
Q_{loss}	Background heat loss, W
Q_{net}	Net dissipated heat, W
Q_{total}	Total input power, W
Re	Reynolds number
r	Flag thickness, μm
s_x/s_y	Displacement in x/y direction, m
$\vec{s}$	Displacement vector, m
tr	Tensor trace
u_{in}	Average inlet air velocity, m/s
u_x/u_y	Velocity in x/y direction, m/s
$\vec{u}$	Velocity vector, m/s
$\vec{\Gamma}$	Stress vector in the airflow, Pa
$\vec{I}$	The unity tensor
$\Delta P/P$	Pressure difference/pressure, Pa
ΔT_{lmtd}	Log mean temperature difference between the copper plate and airflow, K
δR	Experimental uncertainty
δX_i	The uncertainty of one independent variable
η	Performance ratio
λ	Lame's first parameter, Pa
μ	Air dynamic viscosity, kg m^{-1} s^{-1}
μ_s	Lame's second parameter, Pa
ν	Poisson's ratio
ρ	Air density, kg/m^3

ρ_s Flag density, kg/m^3

$\vec{\sigma}$ Stress vector in the flag, Pa

Subscripts

aug Augmentation

c Clean channel

m Modified channel

1. Introduction

High-performance heat sinks are of great significance to the operation of electronic products, which usually generate heat inside. The generated heat may damage the products if it cannot be dissipated effectively. The most commonly used heat sink is an air-cooled system with multiple extended fins forming multiple channels for airflow passing through. However, the flows in such heat sink systems are mostly laminar, which limits the heat transfer efficiency. Many techniques have been tried to enhance the heat transfer, such as making rough surfaces, extending surfaces, or adding twisted tape inside the channels. One effective approach is to add a vortex generator (VG) to make the thermal boundary layer thinner [1–5] by introducing additional turbulence [6]. There are two types of VGs, passive VG and active VG. Passive VGs refer to stationary structures inserted in the channels or attached to the channel wall. A passive VG, which composes of built-in delta winglets, has been shown to improve the heat transfer by 2.5 times [7] or the overall heat dissipation rate by 20-35% [8]. However, a significant pressure drop in the channel was induced, resulting in an unsatisfactory overall efficiency. On the other hand, active VGs involve surface vibration using piezoelectric fans, fluid vibration, or synthetic jets utilizing MEMS [9]. Active VGs cause a lower pressure drop due to their oscillating motions, but all of them demand external power. A forced oscillating cylinder was demonstrated to have 60% enhancement [10] of the channel heat transfer and reduce the pressure drop. However, 300% more mechanical power was needed for its oscillation.

Recently, another technique utilizing aeroelastic flutter has been developed. A flutter is generated by simply inserting some flexible structures into the channels [10–17]. The flexible structure will be self-excited by the flow that improves heat transfer by enhancing core flow mixing. It is similar to the active technique, but no external power is required. It is reported that as high as 300% enhancement in local heat transfer coefficient can be obtained [18]. Even though the core flow mixing increases the channel friction, the benefit of aeroelastic fluttering in heat transfer can still be greater than the negative effect it brought to the channel flow, and

it has been demonstrated in a numerical comparison between the cases of a fixed structure and an oscillating structure [19]. Therefore, more attention was attracted to exploring how to improve heat transfer based on this fluid-structure interaction (FSI) mechanism. Airflow velocity provided by fans for heat sink cooling usually covers a range from 2 m/s to 6 m/s [20]. A key consideration for this FSI technique is the critical velocity, which is the flow velocity that the flag starts flapping. The critical velocity is better to be as low as possible so that the heat transfer improvement can be applied in a wider velocity range [21]. There are three types of flag installation configurations which affect the critical velocity, and they are conventional flags, wall-mounted flags, and inverted flags [22]. The conventional configuration has the flag in line with the incoming flow, with a clamped leading edge and a free trailing edge. The reported heat transfer enhancement is satisfactory [23–28], but its critical velocity is quite high when comparing to the working velocity of heat sinks as mentioned above. In wall-mounted configurations, the flag is clamped on the channel wall and the flag surface is oriented perpendicular to the flow. This configuration causes relatively higher pressure loss than the conventional one due to its spanwise-likely installation [17,29–31].

The inverted configuration is a relatively new approach; it has a flag aligned with the flow but with a free leading edge and a clamped trailing edge. Recently, the aeroelastic instability of this configuration has attracted intensive interest [32–35] because an inverted flag has the lowest critical velocity among all configurations, and its critical velocity can be as low as about 2 m/s [22], which is highly preferred in the heat sink application. However, heat transfer study utilizing an inverted flag is limited [14,15,36,37]. A numerical study is found regarding the heat transfer study by using an inverted flag [36]. In that study, an immersed boundary method was used to analyze the vortical structure and the heat transfer induced by an inverted flag with various bending rigidities. It was shown that the bending rigidity affects the flag dynamics significantly and thus imposes a great influence on convective heat transfer. The bending rigidity is highly dependent on the flag thickness, but experimental study of how thickness

affects heat transfer is still lacking. Heat transfer studies using multiple inverted flags were also found [14,15,37] in the literature, and from those studies, it was suggested that a flag will come across different flag motions along different flow velocities, and the heat transfer performance is highly related to the flag motions. The flag thickness plays a critical role for the flag motion [9], thus in order to understand the heat transfer performance by an inverted flag configuration, investigation of the effect of flag thickness is essential.

To summarize, a flexible vortex generator enhances the heat transfer coefficient in a heat sink, but the high critical velocity constrains its possibility in the application. Seeking ways to lower the critical velocity while keeping the heat transfer performance is needed. This paper studies the heat transfer performance using an inverted flag in a channel flow, which is expected to have a relatively lower critical velocity than other configurations. The flag thickness will affect the heat transfer performance, but it has not been studied experimentally. Therefore, in this work, our objective is to study the flag motion, heat dissipation, friction loss, and thermal-hydraulic performance of an inverted flag configuration under different flow conditions with different flag thicknesses. Firstly, experiments were conducted to investigate the flag motions using a high-speed camera. Second, a series of experiments were carried out to analyze the effects of flag thickness on the heat transfer performance of the channel flow under different flow conditions. Finally, the numerical simulation was applied to analyze the relationship between the vorticity field and the heat transfer performance. Compared with other similar studies, the main novelty of this work is the effect of flag thickness on heat dissipation that has not yet been studied before. The heat transfer performance can be effectively tuned by this simple geometry factor.

2. Experimental method

2.1 Experimental setup

Fig. 1 shows the experimental setup. It consisted of a channel with dimensions of 320 mm (Length) × 30 mm (Width) × 50 mm (Height) made by acrylic plates with a contraction attached to the inlet. The inlet airflow was provided by a wind tunnel (Armfield C15-10), and the velocity was measured by a multi-function ventilation meter (TSI-9565-P-NB). To model a channel inside a heat sink, a uniformly heated copper plate with dimensions of 150 mm (Length) × 50 mm (Height) was embedded into one sidewall of the channel. The copper plate was heated by a heating plate and wrapped by black insulating foam on the back side. Four thermocouples were embedded inside the copper plate to monitor the temperature distribution. The temperature of thermocouples had been calibrated by an isothermal water circulator. A temperature input module (NI 9214) was used to collect the temperatures signals from the thermocouples and transferred the signals to a computer. A temperature controller (Digisense TC9100) was then used to control the temperature of the copper plate by adjusting the heating power, which was recorded by a power meter (RSPM 8213). Inside the channel, a cantilevered flexible flag, which was in the inverted configuration, was placed at the beginning of the test section. There were two pressure tubes in the inlet and outlet of the test section, respectively, for measurement of the differential pressure across the test section by a multi-function ventilation meter (TSI-9565-P-NB). Table 1 shows all parts and components of the experimental setting, including names, models and accuracies with position numbers as shown in Fig. 1(a) and (b).

The sample flags were in the size of 15 mm × 40 mm (Length × Height). Three different thicknesses (r) were studied, i.e., 25 μm, 50 μm and 75 μm. The flags were made of Kapton film with Young's modulus of 2.5 GPa, Poisson ratio of 0.34 and material density of 1.42×10^3 kg/m^3.

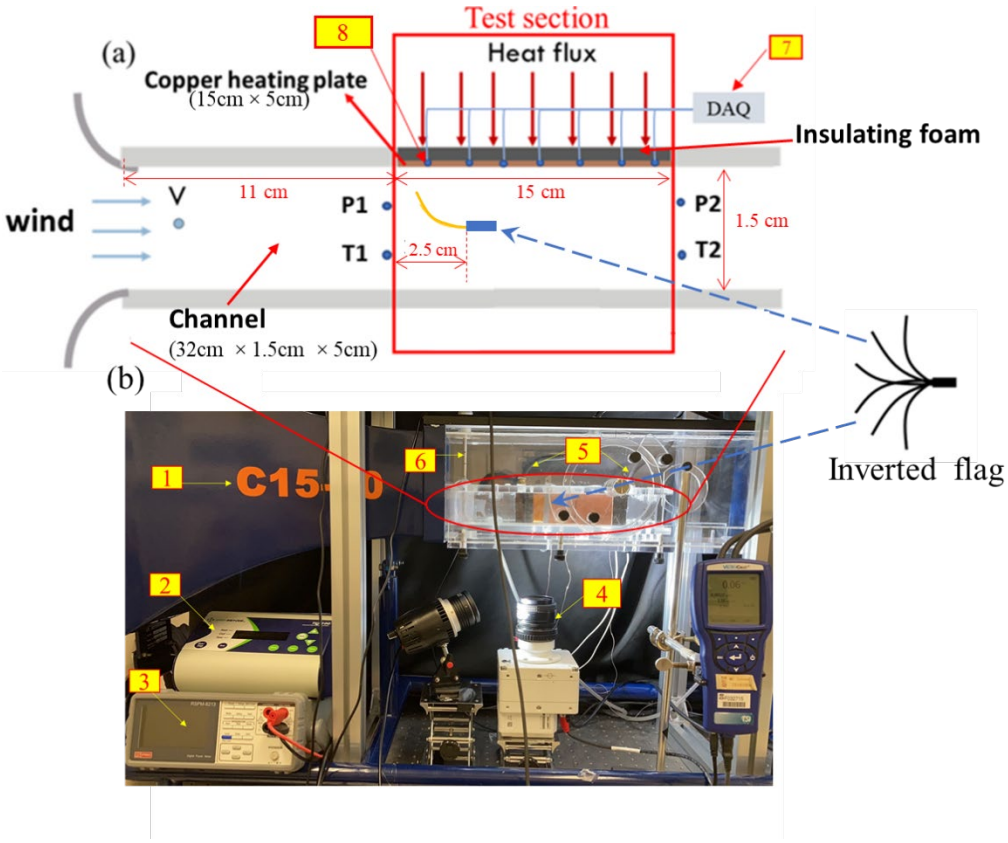

Fig. 1 Schematic diagram and image of the experimental setup. (a) Top view of the setup (schematic); (b) Side view of the setup.

Table 1 Components of the experimental setup.

Number	Name	Model	Measuring range	Accuracies
1	Wind tunnel	C15-10, Armfield	0 to 34 m/s	/
2	Temperature controller	TC9100, Digi-sense	-200 to 1372 °C	±0.5 °C
3	Power meter	RSPM-8213, RS-PRO	0~ >6 kw	± (0.1% of reading + 0.1% of range)
4	High speed camera	VEO 410, Phantom		/
5	Pressure meter	9565-P-NB, TSI	-3735 to 3735 Pa	±1% of reading
6	Velocity meter	9565-P-NB, TSI	1.27 to 78.7 m/s	±3% of reading
7	Data logger	9214, National Instruments		±0.37 °C
8	Thermocouple	K-type, Omega	0 to 260 °C	±0.37 °C

2.2 Experimental procedure and data analysis

The experimental methods are succeeded from our previous work and more details can be referred to [38]. Before the experiment, the setup was preheated for around an hour. During the experiment, the temperature difference between the copper heating plate and the inlet air was maintained at 20 K by automatically tunning the heating plate's input power using the temperature controller. A test was first conducted to estimate the background heat loss. In the background heat loss measurement, the wind speed inside a clean channel (i.e. a channel without flag) was set at zero. A uniform wall temperature at 20 K above the room temperature was maintained on the copper plate. The power consumption of the heater under this setting was recorded by the power meter, and the average value was defined as the background heat loss. The background heat loss at steady state was recorded as Q_{loss}. Then the measurement for the target cases (i.e., clean channel case and cases with different inverted flags) at steady state under different flow velocities were repeatedly conducted. The time-averaged heating power Q_{total} was recorded for each test. The net heat dissipation, Q_{net}, is calculated as follows:

$$Q_{\text{net}} = Q_{\text{total}} - Q_{\text{loss}} \tag{1}$$

The below equation obtains the Reynolds number of the channel flow:

$$\text{Re} = \rho u_{\text{in}} D/\mu \tag{2}$$

where ρ is the air density, u_{in} is the average air velocity through the channel, D is the channel's width, and μ is the air dynamic viscosity. When the flow velocity was increased from 0 to 10 m/s, the Re was increased from 0 to 20800 respectively.

The overall Nusselt number can be calculated by

$$\text{Nu} = hD/k \tag{3}$$

where h is the average heat transfer coefficient, and k is the air thermal conductivity. The average heat transfer coefficient is determined by

$$h = Q_{\text{net}}/\left(\Delta T_{\text{lmtd}} A_{\text{total}}\right) \tag{4}$$

where A_{total} is the total heat transfer area, which is the surface area of the copper plate, ΔT_{lmtd} is the log mean temperature difference between the copper plate and airflow.

Friction factor, f, is calculated by

$$f = 2\Delta PD/(\rho L u_{\mathrm{in}}^2) \tag{5}$$

where ΔP is the streamwise pressure difference between the channel inlet and outlet, and L is the channel length of the test section. The Nusselt number and friction factor augmentations for a given Reynolds number were calculated by the equations below, respectively.

$$\mathrm{Nu_{aug}} = \mathrm{Nu_m}/\mathrm{Nu_c} \tag{6}$$

$$f_{\mathrm{aug}} = f_{\mathrm{m}}/f_{\mathrm{c}} \tag{7}$$

where the subscripts m and c represent the modified and clean channels, respectively.

In order to consider the power consumption due to the pressure drop, the performance ratio η, is introduced to compare the heat transfer enhancement at constant pumping power, i.e., $(\Delta P u_{\mathrm{in}})_{\mathrm{m}}=(\Delta P u_{\mathrm{in}})_{\mathrm{c}}$. This performance factor is calculated as below [39,40].

$$\eta = \mathrm{Nu}/\mathrm{Nu_c^*} \tag{8}$$

where Nu_c^* is the Nusselt number of the clean channel evaluated at the velocity defined by the same pumping power condition.

During the experiment, a high-speed camera (Phantom VEO410) was used to capture the motion of the flag. To ensure enough contrast for identification, flag edges were painted white while the flag surface was painted black [22,38]. The flag motion envelope was constructed by superimposing the recorded high-speed video frames.

The experimental uncertainty was evaluated as below [38,41].

$$\delta R = \left[\sum_{\mathrm{i}}^{\mathrm{N}} \left(\frac{\partial R}{\partial X_{\mathrm{i}}}\delta X_{\mathrm{i}}\right)^2\right]^{1/2} \tag{9}$$

where δX_{i} represents the uncertainty of one independent variable. Table 1 shows the measurement accuracies associated with the experimental components. The uncertainties were 3% for the Reynold number, 5% for the friction factor, and less than 2.5% for the Nusselt number.

3. Numerical method

3.1 Model description

In the current study, the heat transfer results were measured through experiments. We hypothesize that a small variation in flag thickness triggers great changes in the flow field, like the vorticity, thus impacting the heat transfer. The most direct method to capture the flow field shall be through experiment. However, due to the quick flapping of the flag, it is difficult to capture the flow field around the flag. Thus, to validate our hypothesis, we designed the simulation which is mainly for analyzing the flow field.

In the experiment, a high-speed camera was used to investigate the flag motion and found that the flag was basically in 2D fluttering as shown in Section 4.1. Since the aim of the simulation is to examine the flow field for testing our hypothesis, and the dramatic computational resource demanded by 3D simulation (130k grids in 2D *vs* 130000k grids in 3D), 2D simulation was used in this study, and the 3D simulation will be left to the future work. Moreover, in the experiment, the flow entering into the channel was provided by a wind tunnel and was laminar. Since the channel was shorter than the required entrance length for turbulence to be fully developed, the flow may be in the laminar or transition stage, and it is difficult to find a suitable turbulence model for simulations to resemble the experiment. Therefore, the model employed in the simulation was a laminar model, and validation will be given in Section 3.2.

The 2D physical model is shown in Fig. 2(a), which represents the top-view of the experimental setup, and the dimensions are the same as those in the experimental setting. Nonslip top and bottom boundary conditions were applied. A parabolic profile with an average velocity u_{in} was set at the inlet, and ambient pressure P_{ambient} was assumed at the outlet. An inverted flag was installed inside the channel. The governing equations for the air flow are

$$\frac{\partial u_{\text{x}}}{\sigma x} + \frac{\partial u_{\text{y}}}{\partial y} = 0 \tag{10}$$

$$\rho\left(\frac{\partial u_{\mathrm{x}}}{\partial t}+u\frac{\partial u_{\mathrm{x}}}{\partial x}+v\frac{\partial u_{\mathrm{x}}}{\partial y}\right)=-\frac{\partial P}{\partial x}+\mu\left(\frac{\partial^2 u_{\mathrm{x}}}{\partial x^2}+\frac{\partial^2 u_{\mathrm{x}}}{\partial y^2}\right) \tag{11}$$

$$\rho\left(\frac{\partial u_{\mathrm{y}}}{\partial t}+u\frac{\partial u_{\mathrm{y}}}{\partial x}+v\frac{\partial u_{\mathrm{y}}}{\partial y}\right)=-\frac{\partial P}{\partial y}+\mu\left(\frac{\partial^2 u_{\mathrm{y}}}{\partial x^2}+\frac{\partial^2 u_{\mathrm{y}}}{\partial y^2}\right) \tag{12}$$

$$\begin{cases} At\ x=0, \quad u_{\mathrm{x}}=1.5u_{\mathrm{in}}\left(1-\left(\frac{y}{0.5H}\right)^2\right), \quad u_{\mathrm{y}}=0, \\ At\ x=L, \quad P=P_{\mathrm{ambient}} \\ At\ y=-0.5H, \quad u_{\mathrm{x}}=0, \quad u_{\mathrm{y}}=0 \\ At\ y=0.5H, \quad u_{\mathrm{x}}=0, \quad u_{\mathrm{y}}=0 \end{cases} \tag{13}$$

where u_{x} and u_{y} are the velocities in x and y-direction, respectively, H is the channel width, and P is the air pressure. All air properties were set as the same as those in the experiments.

Based on Newton's second law of motion, the oscillation of the two-dimensional flag can be described as,

$$(\lambda+\mu_s)\nabla(\nabla\cdot\vec{s})+\mu_s\Delta\vec{s}=\rho_s\frac{\partial^2\vec{s}}{\partial t^2} \tag{14}$$

where $\vec{s}=\left[s_{\mathrm{x}},s_{\mathrm{y}}\right]^T$ is the displacement, ρ_{s} is the flag density, λ and μ_{s} are Lame constants, which are linked to Young's modulus E and Poisson's ratio ν by

$$\lambda=\frac{\nu\mathrm{E}}{(1+\nu)(1-2\nu)} \tag{15}$$

$$\mu_{\mathrm{s}}=\frac{E}{2(1+\nu)} \tag{16}$$

All the flag material properties are the same as those in experiments. The continuous boundary conditions on the flag surface is as below.

$$\begin{cases} \vec{v}=\dfrac{\partial\vec{s}}{\partial t} \\ \vec{\sigma}\cdot\vec{n}=\vec{\Gamma}\cdot\vec{n} \end{cases} \tag{17}$$

where $\vec{\sigma}$ is the stress tensor in the solid and $\vec{\Gamma}$ is the stress tensor in the fluid with $\vec{u}=\left[u_{\mathrm{x}},u_{\mathrm{y}}\right]^T$.

$$\vec{\sigma}=\mu_s[(\nabla\vec{s})^T+\nabla\vec{s}]+\frac{\lambda}{2}tr[(\nabla\vec{s})^T+\nabla\vec{s}]\vec{I} \tag{18}$$

$$\vec{\Gamma}=-P\vec{I}+\mu[(\nabla\vec{u})^T+\nabla\vec{u}]-\frac{2}{3}\mu(\nabla\cdot\vec{u})\vec{I} \tag{19}$$

Here *tr* is the tensor trace, and $\vec{I}$ is the unity tensor.

COMSOL Multiphysics was used to solve the above governing equations. The Arbitrary Lagrangian-Eulerian method in COMSOL enables the automated bidirectional coupling of fluid flow and structural deformation.

3.2 Model validation and grid-independence study

To verify the numerical model, the benchmark case of Turek and Hron [42] was calculated, and compared with others [42,43]. In the case, an elastic beam was attached to a fixed cylinder inside a channel, as shown in Fig. 2(b). Nonslip conditions were defined at the top and bottom boundaries, while a parabolic velocity profile was set at the inlet. The flow Reynolds number was 100, and the ratio of the structure to fluid densities was $\rho_s \,/\, \rho_f = 10$. The dimensionless Young's Modulus was $E^* = E \,/\, \rho_f u_{\mathrm{in}}^2 = 1400$.

Fig. 2(c) shows the calculation of the beam tip's horizontal and vertical displacements at different times. After a 6s transient state, the beam exhibited harmonic oscillations with constant frequency and amplitude. The mean position, amplitude, and frequency of oscillation in both *x* and *y* directions are compared with results in the literature [42,43], as shown in Fig. 2(d). Good agreements were found.

A grid-independence study was performed. Four different grids were used to solve our target problem, which was described in Fig. 2(a). The mean velocity was defined as 4 m/s, and the flag thickness was 25 μm. The channel wall vorticity was used for grid analysis. The result of grid-independence study is shown in Fig. 2(e). Grid 4, as shown in Fig. 2(f), was chosen in this work to save computational resources while maintaining good accuracy. Specifically, the airflow domain was discretized with 120254 triangular cells and 7434 quadrilateral cells. The

mesh was refined at channel wall boundaries and the fluid-structure interface. The flag domain consisted of 3160 triangular cells.

The numerical results were also compared with the experimental results as shown in Fig. 2(g-i). Fig. 2(g) shows the flag tip displacement from the numerical case of r = 75 μm in the average velocity of 6.5 m/s, and the numerical flag amplitude was taken from the y displacement. Fig. 2(h) shows the corresponding experimental flag flapping envelop, and the experimental flag flapping amplitude was measured as shown in the figure. Fig. 2(i) shows the comparison of the numerical results and the experimental results for the cases that flags were undergoing the critical transition. The results of the critical velocity, the flag flapping frequency, and the flag amplitude between simulations and experiments agree very well.

Model configuration

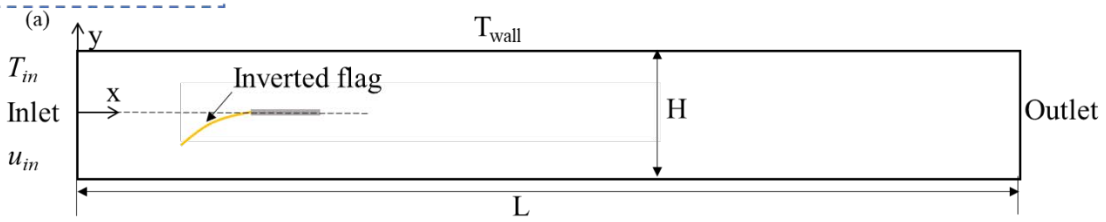

Model validation with a benchmark case

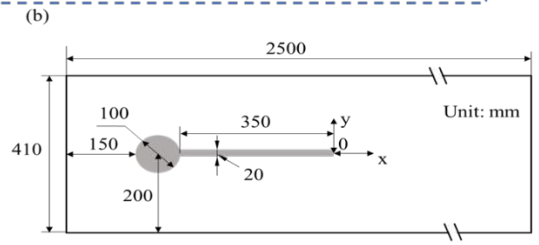

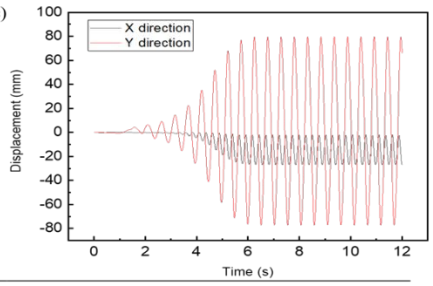

(d)

	x direction			y direction		
	Present results	Turek and Hron	Ali et.al	Present results	Turek and Hron	Ali et.al
Mean position (mm)	1.40	-14.58	-14.56	1.28	1.23	1.30
Amplitude (mm)	12.79	12.44	12.58	79.73	80.06	81.05
Frequency (Hz)	3.85	3.80	3.75	1.95	2.0	1.90

Model grid-independence study

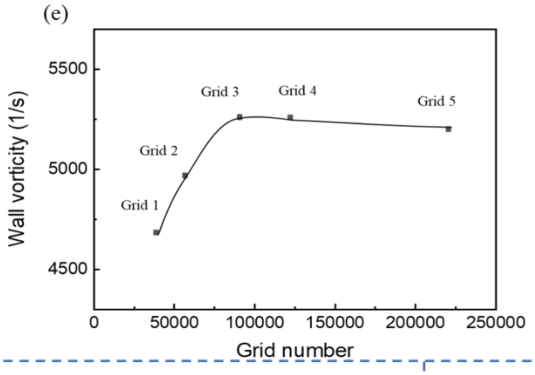

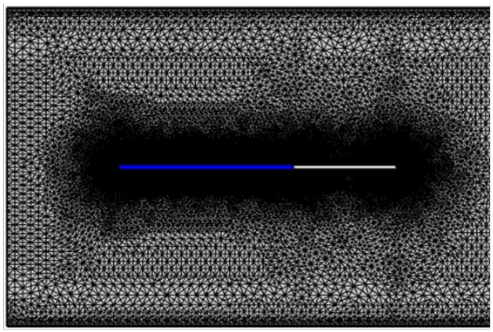

Model validation with experiments

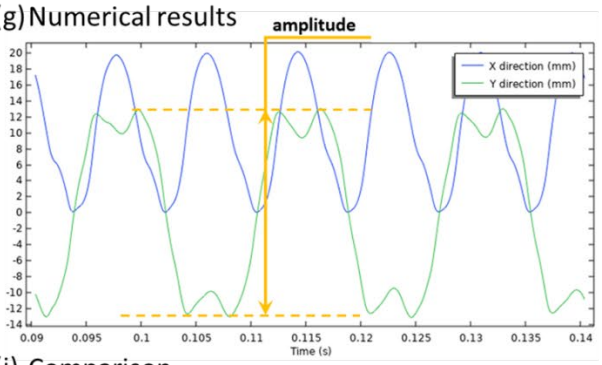

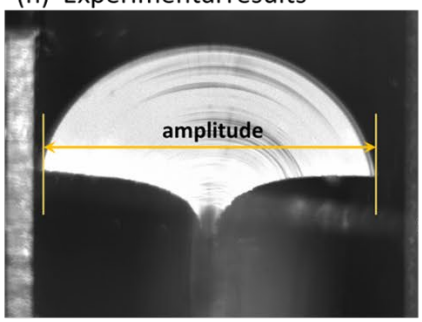

(i) Comparison

Simulation				Experiment			
flag thickness (μm)	velocity (m/s)	flapping frequency (Hz)	amplitude (cm)	flag thickness (μm)	velocity (m/s)	flapping frequency (Hz)	amplitude (cm)
25	1.5	14.29	2.50	25	1.6	15.15	2.68
50	4	33.34	2.60	50	4.12	35.71	2.45
75	6.5	61.54	2.55	75	6.54	63.83	2.65

Fig. 2. Details of the numerical model. (a) Physical model of an inverted flag in the channel flow; Model validation parts including (b) Computational domain for the validation case, (c) Horizontal and vertical displacement for the validation case, and (d) Model validation results; Model grid-independent study including (e) The comparison of different grids results, (f) The grid used in the simulation (only the former part that has the flag is shown). (g) Numerical result showing the flag tip displacement versus time, (h) Experimental result showing the flag flapping envelop, (i) Comparison between simulation and experiment regarding the flag motion.

4. Results and Discussion

4.1 Effects on flapping dynamics

A high-speed camera was used to study the motion of the inverted flag installed in the channel as described in Section 2.1. It was found that the motion can be classified into three typical modes, as shown in Fig. 3(a): (1) the straight mode when the flag keeps its original shape and stays static; (2) the flapping mode when the flag flaps; and (3) the deflected mode when the flag is forced to turn to one side. The motion modes of an inverted flag are related to the channel velocity and the flag thickness. As shown in Fig. 3(b), when the velocity increases, generally, an inverted flag exhibits the straight mode, flapping mode, and finally deflected mode in sequence. The flags with thickness of r = 25 μm and that of r = 50 μm exhibit all three modes as the flow velocity increases from 0 to 10 m/s, while the flag with r = 75 μm only exhibits two modes up to 10 m/s. In the deflected mode, the r=25 μm flag flaps again due to its high flexibility, when the velocity is large enough. Fig. 3(b) clearly shows that under the same channel velocity, flags with different thicknesses perform different motions, indicating that the flag thickness strongly affects the flag motion.

The transition from the straight mode to the flapping mode is the most important phenomenon to be studied, and it happens at a lower velocity for a thinner flag. The transition velocity is generally named the critical velocity. The critical velocities are about 1.5 m/s, 4 m/s, 6.5 m/s for r=25 μm, r=50 μm, r=75 μm flags, respectively. It is reasonable for a thinner flag having a lower critical velocity because the flag thickness is related to the bending rigidity, i.e., a thicker flag has a higher bending rigidity, and requires more flow power to induce enough disturbance for oscillation. Compared with flags in the same size under the conventional configuration, of which critical velocities are normally beyond 10 m/s, the r = 25 μm inverted flag achieved the lowest critical velocity of about 1.5 m/s, indicating its potential advantages as a vortex generator in the heat sink application, where a low working velocity is preferred.

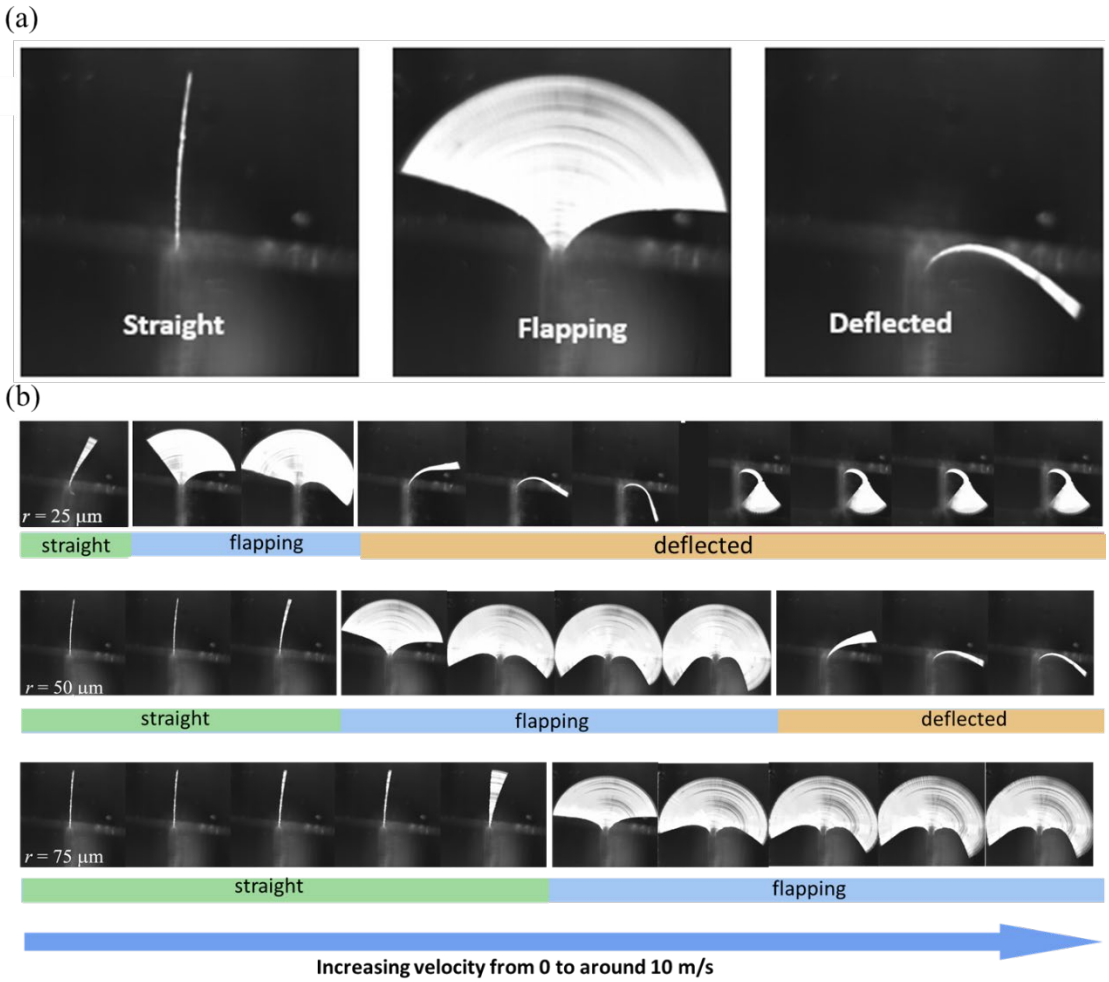

Fig. 3. Details of flag motion. (a) Three typical flag motion modes; (b) Flag mode development as a function of increasing airflow velocity for r = 25 μm flag, r = 50 μm flag, and r = 75 μm flag.

4.2 Effects on flow friction

Fig. 4(a) shows the results of pressure drop for different cases. The pressure drop of the clean channel case slowly increases with the Reynolds number. For the other three cases (with flags), the pressure drops of the channel are similar to the clean channel case in the low-Re regime (Re < 5000), where the flags have not flapped. When the flags start flapping, the pressure drops increase with a significantly larger slope than that in the clean channel case. As flow velocity increases, their pressure drops increase. For the channel with 50 μm flag, a jump of pressure drop was observed at the transition from the straight to flapping modes, and then the rate of increase of pressure drop changed at the transition from the flapping to deflected modes. The jump of pressure drop at the straight-flapping transition was more prominent for the case of 75 μm flag, while it is less obvious for the case of 25 μm flag. So, the increase in pressure drop at the mode transition is highly related to the flag thickness.

The results of pressure drop can be reinterpreted into a dimensionless parameter as the friction factor. Fig. 4(b) shows the results of friction factors for different cases. For the clean channel case, the friction factor slowly decreases as the Reynolds number increases. For the cases with flags, the highest friction factor for each case happens at the transition from the straight mode to the flapping mode. An increase of friction factor at the second transition from the flapping mode to the deflected mode can be observed through the case of r = 50 μm flag.

Fig. 4(c) summarizes the friction factor augmentation against the Reynolds number for the cases with flags. The largest increase in friction factor for each case happens at the straight-

flapping mode transition. The r=25 μm flag has the lowest critical velocity and induces the lowest friction augmentation, while for a thicker flag, a higher critical velocity and a larger friction augmentation are obtained.

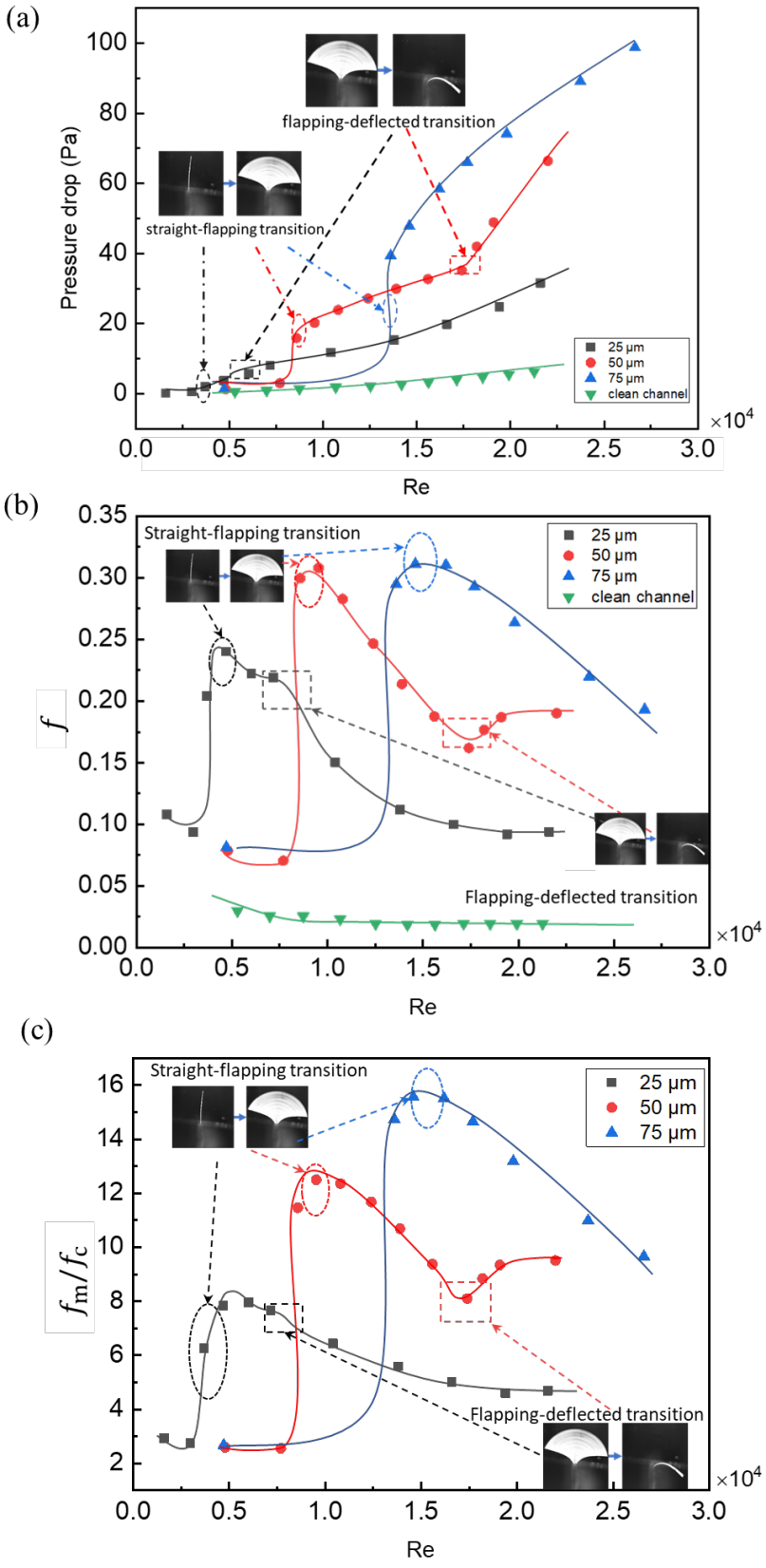

Fig. 4. Effects of flag thickness on flow friction. (a) Pressure drop; (b) friction factor; (c)

friction augmentation with the increase in Re

4.3 Effects on heat transfer and thermal-hydraulic performance

Fig. 5(a) shows the relationship between the Nusselt number and the Reynolds number for different cases. For the clean channel case, the Nusselt number monotonically increases with the Reynolds number. For the other three cases with flags, before the straight-flapping mode transition, the Nusselt number was slightly higher than that of the clean channel, because even when the flags have not yet flapped, they have already worked as rigid vortex generators, thus enhanced the heat transfer.

As the Reynolds number increases, the Nusselt numbers for the cases with flags have a large jump during the straight-flapping mode transition, resulting in a significant enhancement of heat dissipation compared with the clean channel case. When the Reynolds number goes higher, until in the flapping-deflected mode transition, as illustrated by the r = 50 μm flag case (Re=17000), the Nusselt number drops a bit and increases again, but still larger than that of the clean channel case. It is because the flag in deflected mode, no matter flapping or not, acts like a vortex generator in the channel, thus, the channel with the deflected flag can still have a higher heat dissipation effect than the clean channel.

Fig. 5(b) shows the plot of Nusselt number augmentation for the cases with flags. The peak values appear at the straight-flapping mode transition. The highest Nusselt number augmentations for the cases with r = 25 μm, 50 μm and 75 μm flags are 1.68, 2.02, and 1.84, respectively. It suggests that if the hydraulic loss is not considered, the case with the r=50 μm flag achieves the highest heat transfer enhancement among all cases, and the enhancement is obtained around the flag critical velocity. After the first mode transition, the augmented heat dissipation effect for all the cases gradually decreases with the Reynolds number.

In order to consider the hydraulic loss, Fig. 5(c) shows the performance ratio η as defined in Eq. (8) for the three cases with flags. Generally, when flags have not yet flapped, η is less than 1, which means that the induced friction overrides the heat transfer enhancement brought by the straight-mode flag. The peak η for all the cases happens at around the straight-flapping mode transition, which means that the best performance occurs when flags start flapping. At that moment, the channel Nusselt number has a huge jump while the channel friction increases moderately. After the peak, as the Reynolds number increases, η decreases because of the gradual increase of friction and the great decrease of heat transfer enhancement, which is due to the thinned thermal boundary layer between the heating copper plate and the ambient airflow. Detailed analysis was presented in the next section. In this study, the maximum η is 1.16 for the case with the r = 25 μm flag, which happens at around Re = 3500. It is noted that in our previous work [38], the flag of the same thickness (25 μm) in conventional configuration does not flap at low wind speed until reaching its critical velocity at 7 m/s, while a significant heat transfer enhancement can be achieved by the inverted flag in this work in wind speed as low as 1.5 m/s. Therefore, this inverted configuration is suggested to be used for the low-speed regime and the conventional configuration is preferred for the high-speed regime.

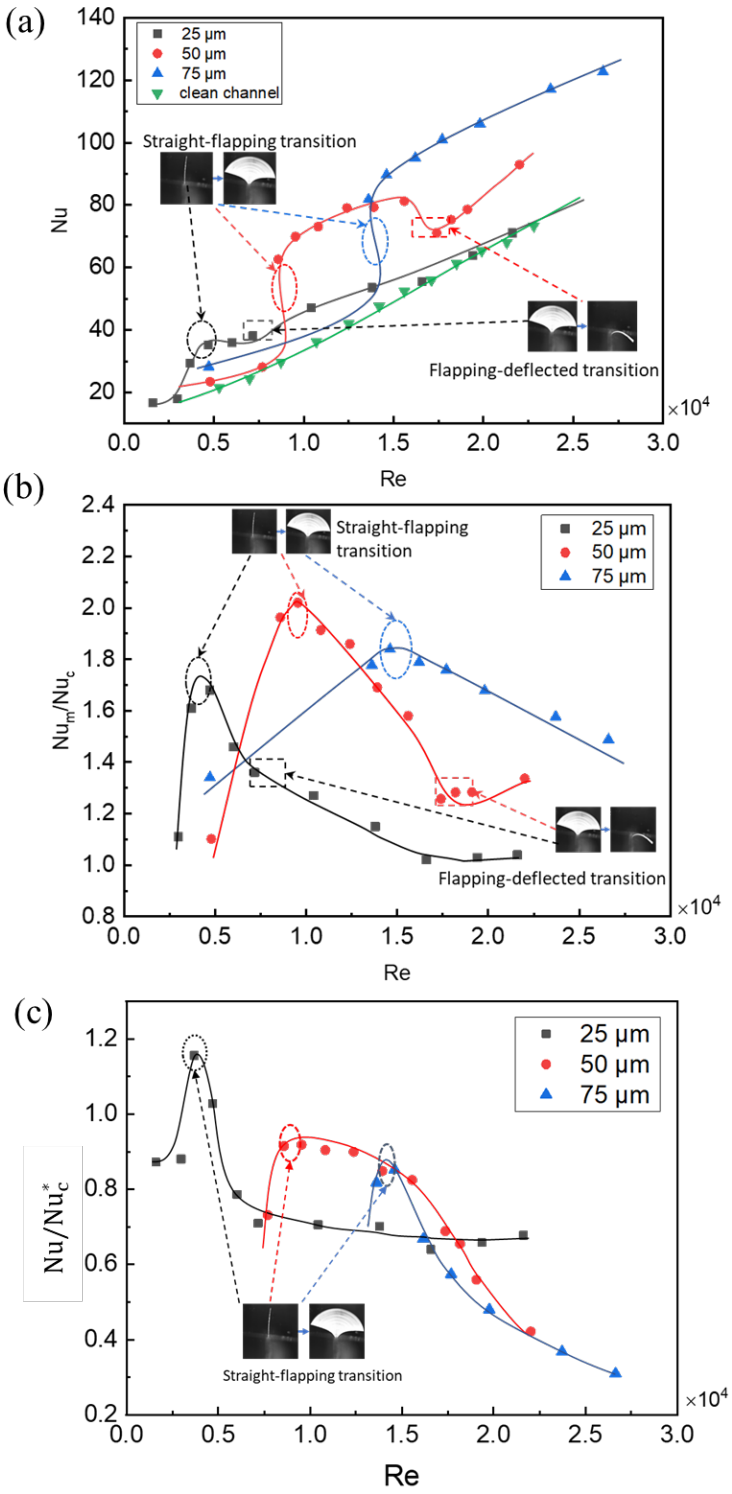

Fig. 5. Effect of flag thickness on heat transfer. (a) Average Nusselt number, (b) Nu augmentation and (c) Performance ratio.

4.4 Numerical study of flag motion-related vorticity and its effect on heat transfer

The experimental results presented in previous sections indicate that the channel heat transfer enhancement is highly related to the flag motion modes and the flag thickness. To better understand the mechanism, the vorticity fields for the four cases (i.e., clean channel case, and three cases with flags of different thicknesses) at different Reynolds numbers were investigated by simulation, as shown in Fig. 6.

Fig. 6(a) shows the vorticity fields of different cases at Re = 8300. For r = 25, 50 and 75 μm, the flags are at the deflected mode, flapping mode and straight mode respectively. The vorticity fields are nearly constant with time for the case of r = 75 μm flag and for the clean channel case. For the cases of r = 25 μm and r = 50 μm flags, the vorticity fields are time-varying, and the eddies are propagating downstream, while the r = 50 μm flag induces more and stronger vortices than the r = 25 μm one. Since the heat transfer increases significantly when the fluid vortex approaches the wall [44], the vorticity on the channel wall was thus extracted and summarized in Fig. 6(b-d). When Re = 8300 (Fig. 6c), for the channel with the r = 50 μm flag, which is at the flapping mode, its vorticity enhancing effect is the strongest around where the flag is installed, while for the rest of the channel wall, the vorticity enhancement is not obvious. Under the same Re, the wall vorticity for the cases of r = 25 μm and r = 75 μm is limited, at which they are in deflected flag mode and straight flag mode, respectively. For the other two flow conditions, when Re = 3130 (Fig. 6b) and Re = 14600 (Fig. 6d), similar results were found. At Re = 3130, the r = 25 μm flag is in the flapping mode, and it has the highest vorticity around the flag position, while the vorticities for the cases of other flag thicknesses are very small. At Re = 14600, the vorticity of the case of r = 75 μm which is in flapping flag mode, is much higher than the others. Therefore, it is concluded that flags in the flapping mode generate the largest vorticity around the flag position compared with flags in other modes.

The average vorticity, which is averaged in one period of cycle and then averaged along the

channel wall, is also extracted and summarized in Fig. 6(e). For different Reynolds numbers, the four cases show different average vorticities. When the straight-flapping mode transition happens, the channel vorticity has a strong enhancement. On the other hand, the magnitude of the average vorticity has an obvious drop when the flag undergoes the flapping-deflected transition. Both observations are consistent with the experimental results about the effects on heat transfer and thermal-hydraulic performance as discussed in Section 4.3. By comparing Fig. 6(e) with Fig. 5(a), their overall trends are very similar, especially for the regime at $Re < 15000$. This suggests that the vorticity enhancement is highly related to the heat transfer enhancement at the low-Re regime. When Re increases (e.g. $Re > 15000$), the thermal boundary layer becomes thinner, and the effect of vorticity enhancement on heat transfer enhancement is less significant at high-Re regime.

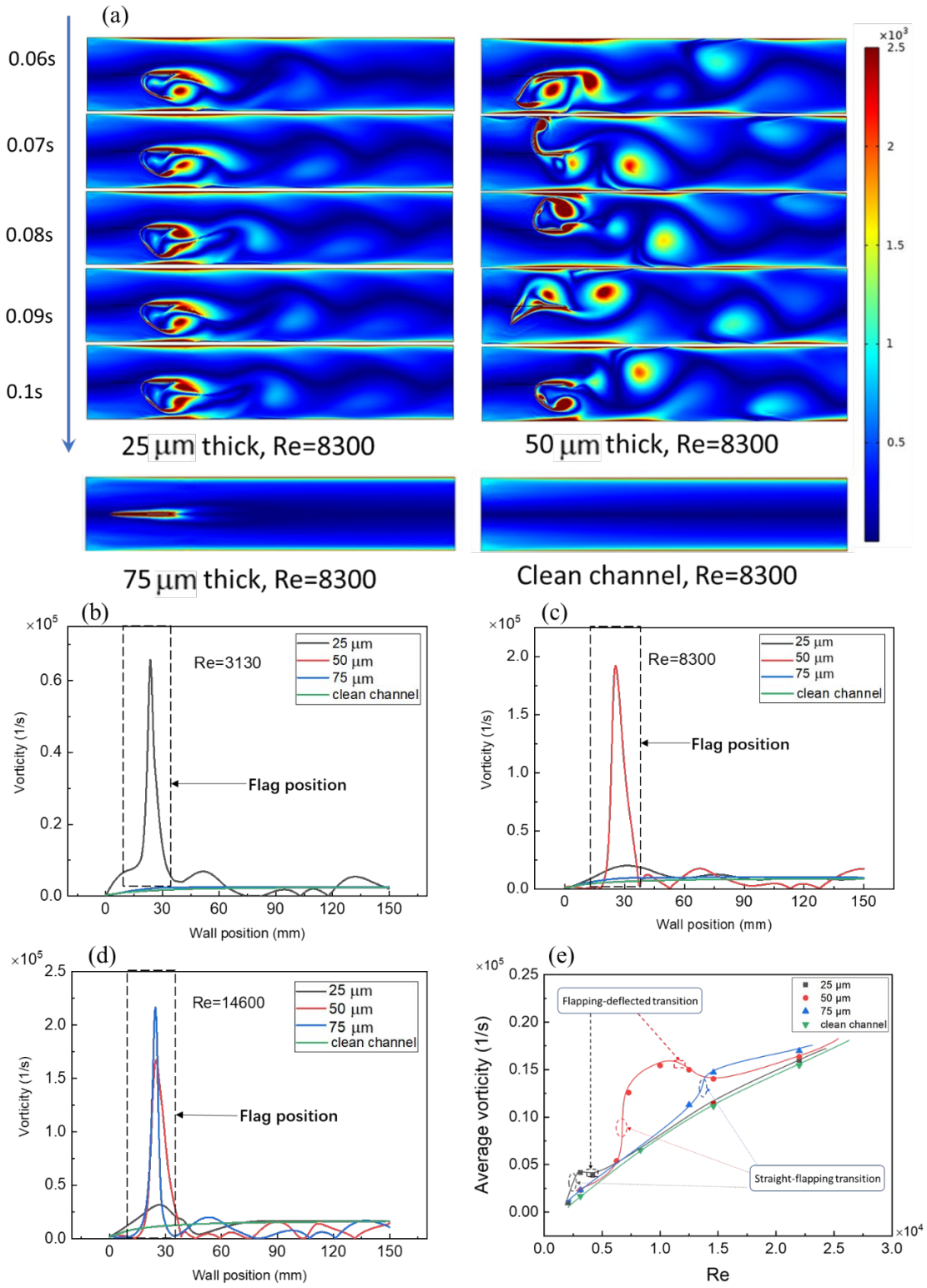

Fig. 6. Flag motion-related vorticity and its effect on heat transfer. (a) Comparison of visual vorticity field for different flags at Re = 8300; (b) Comparison of wall vorticity for different flags at Re = 8300; (c) Comparison of wall vorticity for different flags at Re = 3130; (d)

Comparison of wall vorticity for different flags at Re = 14600; (e) Comparison of average vorticity for different flags at different Re.

5. Concluding Remarks

In this work, the inverted flag motion, the Nusselt number, the friction factor, and the thermal-hydraulic performance of a channel flow with an inverted flag were examined with different flag thicknesses and flow Reynolds numbers. Three different motion modes are identified: straight, flapping, and deflected modes. The flapping motion of the flag yields the increase in flow friction, and the highest flow friction occurs at the straight-flapping mode transition. The Nu augmentation achieves as high as 200% compared with the clean channel. The numerical simulation shows the high dependence of the flag motion on the wall vorticity. The largest vorticity was observed under the flapping mode, leading to the highest heat dissipation effect compared with other two modes. The enhancement of thermal-hydraulic performance is 16% and appears at the straight-flapping mode transition for the thinnest flag with a thickness of 25 μm. Besides, the critical velocity is as low as 1.5 m/s, which is far lower to the conventional flag. Therefore, the high potential in enhancing the heat dissipation performance by inserting inverted flags into heat sinks was realized in this work, including lower critical velocity and superior heat transfer performance.

6. Acknowledgements

This work was supported by the grants from the Research Grants Council of the Hong Kong Special Administrative Region, China (GRF Project Nos.17205419 & 17203220).

7. References

[1] F.A.S. da Silva, D.J. Dezan, A. V Pantaleao, L.O. Salviano, Longitudinal vortex generator applied to heat transfer enhancement of a flat plate solar water heater, Applied Thermal Engineering. 158 (2019) 113790.

[2] Y. Zheng, H. Yang, H. Mazaheri, A. Aghaei, N. Mokhtari, M. Afrand, An investigation on the influence of the shape of the vortex generator on fluid flow and turbulent heat transfer of hybrid nanofluid in a channel, Journal of Thermal Analysis and Calorimetry. 143 (2021) 1425–1438.

[3] M. Samadifar, D. Toghraie, Numerical simulation of heat transfer enhancement in a plate-fin heat exchanger using a new type of vortex generators, Applied Thermal Engineering. 133 (2018) 671–681.

[4] U. Kashyap, K. Das, B.K. Debnath, Effect of surface modification of a rectangular vortex generator on heat transfer rate from a surface to fluid: An extended study, International Journal of Thermal Sciences. 134 (2018) 269–281.

[5] C. Zhai, M.D. Islam, R. Simmons, I. Barsoum, Heat transfer augmentation in a circular tube with delta winglet vortex generator pairs, International Journal of Thermal Sciences. 140 (2019) 480–490.

[6] T.L. Bergman, F.P. Incropera, D.P. DeWitt, A.S. Lavine, Fundamentals of heat and mass transfer, John Wiley & Sons, 2011.

[7] S. Tiwari, P.L.N. Prasad, G. Biswas, A numerical study of heat transfer in fin- tube heatexchangers using winglet-type vortex generators in common-flow down configuration, Progress in Computational Fluid Dynamics, an International Journal. 3 (2003) 32–41.

[8] M.S. Sohal, Improving Vortex Generators to Enhance the Performance of Air-Cooled Condensers in a Geothermal Power Plant, Idaho National Laboratory (INL), 2005.

[9] R.K.B. Gallegos, R.N. Sharma, Flags as vortex generators for heat transfer enhancement: Gaps and challenges, Renewable and Sustainable Energy Reviews. 76 (2017) 950–962.

[10] J. Fu, C. Hefler, H. Qiu, W. Shyy, Effects of aspect ratio on flapping wing aerodynamics in animal flight, Acta Mechanica Sinica. 30 (2014) 776–786.

[11] K. Shoele, R. Mittal, Flutter instability of a thin flexible plate in a channel, Journal of Fluid Mechanics. 786 (2016) 29–46.

[12] J. Fu, W. Shyy, H. Qiu, Effects of aspect ratio on vortex dynamics of a rotating wing, AIAA Journal. 55 (2017) 4074–4082.

[13] J. Fu, X. Liu, W. Shyy, H. Qiu, Effects of flexibility and aspect ratio on the aerodynamic performance of flapping wings, Bioinspiration & Biomimetics. 13 (2018) 36001.

[14] Y. Chen, Y. Yu, W. Zhou, D. Peng, Y. Liu, Heat transfer enhancement of turbulent channel flow using tandem self-oscillating inverted flags, Physics of Fluids. 30 (2018) 75108.

[15] Y. Chen, Y. Yu, D. Peng, Y. Liu, Heat transfer enhancement of turbulent channel flow using dual self-oscillating inverted flags: Staggered and side-by-side configurations, International Journal of Heat and Mass Transfer. 136 (2019) 851–863.

[16] R.K.B. Gallegos, R.N. Sharma, Heat transfer performance of flag vortex generators in rectangular channels, International Journal of Thermal Sciences. 137 (2019) 26–44.

[17] Z. Li, X. Xu, K. Li, Y. Chen, G. Huang, C.L. Chen, C.H. Chen, A flapping vortex generator for heat transfer enhancement in a rectangular airside fin, International Journal of Heat and Mass Transfer. 118 (2018) 1340–1356.

[18] P. Hidalgo, A. Glezer, Small-Scale Vorticity Induced by a Self-Oscillating Fluttering Reed for Heat Transfer Augmentation in Air Cooled Heat Sinks, in: International Electronic Packaging Technical Conference and Exhibition, American Society of Mechanical Engineers, 2015: pp. IPACK2015-48511, V001T09A004.

[19] A.K. Soti, R. Bhardwaj, J. Sheridan, Flow-induced deformation of a flexible thin structure as manifestation of heat transfer enhancement, International Journal of Heat and Mass Transfer. 84 (2015) 1070–1081.

[20] AVC'S Product/Fans & Blowers, (1991). http://www.avc.co/en-us/ProductTechnology/fan (accessed January 13, 2022).

[21] R.K.B. Gallegos, R.N. Sharma, Flags as vortex generators for heat transfer enhancement: Gaps and challenges, Renewable and Sustainable Energy Reviews. 76 (2017) 950–962.

[22] Z. Dou, A. Rips, L. Jacob, R. Mittal, Experimental characterization of the flow-induced

flutter of a suspended elastic membrane, AIAA Journal. 58 (2020) 445–454.

[23] C. Eloy, N. Kofman, L. Schouveiler, The origin of hysteresis in the flag instability, Journal of Fluid Mechanics. 691 (2012) 583–593.

[24] M. Bryant, E. Wolff, E. Garcia, Aeroelastic flutter energy harvester design: the sensitivity of the driving instability to system parameters, Smart Materials and Structures. 20 (2011) 125017.

[25] Z. Pang, L. Jia, X. Yin, Flutter instability of rectangle and trapezoid flags in uniform flow, Physics of Fluids. 22 (2010) 121701.

[26] C. Eloy, R. Lagrange, C. Souilliez, L. Schouveiler, Aeroelastic instability of cantilevered flexible plates in uniform flow, Journal of Fluid Mechanics. 611 (2008) 97–106.

[27] L. Tang, M.P. Paı¨doussis, On the instability and the post-critical behaviour of two-dimensional cantilevered flexible plates in axial flow, Journal of Sound and Vibration. 305 (2007) 97–115.

[28] T.S. Balint, A.D. Lucey, Instability of a cantilevered flexible plate in viscous channel flow, Journal of Fluids and Structures. 20 (2005) 893–912.

[29] K. Li, S. Wang, Z. Ke, C.L. Chen, A novel caudal-fin-inspired hourglass-shaped self-agitator for air-side heat transfer enhancement in plate-fin heat exchanger, Energy Conversion and Management. 187 (2019) 297–315.

[30] S. Wang, K. Li, Z. Ke, C.L. Chen, Time-resolved PIV measurement and thermal-hydraulic performance evaluation of thin film self-agitators in a rectangular channel flow, International Journal of Heat and Mass Transfer. 137 (2019) 922–939.

[31] S. Wang, R. Enyard, K. Li, C.L. Chen, Inverted structurally inhomogeneous stepped agitators in a channel flow, International Journal of Heat and Mass Transfer. 159 (2020) 120094.

[32] J. Ryu, S.G. Park, B. Kim, H.J. Sung, Flapping dynamics of an inverted flag in a uniform flow, Journal of Fluids and Structures. 57 (2015) 159–169.

[33] H. Huang, H. Wei, X.-Y. Lu, Coupling performance of tandem flexible inverted flags in

a uniform flow, Journal of Fluid Mechanics. 837 (2018) 461–476.

[34] C. Tang, N.-S. Liu, X.-Y. Lu, Dynamics of an inverted flexible plate in a uniform flow, Physics of Fluids. 27 (2015) 73601.

[35] P.S. Gurugubelli, R.K. Jaiman, Self-induced flapping dynamics of a flexible inverted foil in a uniform flow, Journal of Fluid Mechanics. 781 (2015) 657–694.

[36] S.G. Park, B. Kim, C.B. Chang, J. Ryu, H.J. Sung, Enhancement of heat transfer by a self-oscillating inverted flag in a Poiseuille channel flow, International Journal of Heat and Mass Transfer. 96 (2016) 362–370.

[37] Y. Yu, Y. Liu, Y. Chen, Vortex dynamics and heat transfer behind self-oscillating inverted flags of various lengths in channel flow, Physics of Fluids. 30 (2018) 45104.

[38] X.L. Zhong, S.C. Fu, K.C. Chan, G. Yang, H.H. Qiu, C.Y.H. Chao, Experimental study on the thermal-hydraulic performance of a fluttering split flag in a channel flow, International Journal of Heat and Mass Transfer. 182 (2022) 121945.

[39] T.M. Liou, J.J. Hwang, Effect of ridge shapes on turbulent heat transfer and friction in a rectangular channel, International Journal of Heat and Mass Transfer. 36 (1993) 931–940.

[40] R. Karwa, C. Sharma, N. Karwa, Performance Evaluation Criterion at Equal Pumping Power for Enhanced Performance Heat Transfer Surfaces, Journal of Solar Energy. 2013 (2013) 1–9.

[41] R.J. Moffat, Describing the uncertainties in experimental results, Experimental Thermal and Fluid Science. 1 (1988) 3–17.

[42] S. Turek, J. Hron, Proposal for numerical benchmarking of fluid-structure interaction between an elastic object and laminar incompressible flow, in: Fluid-Structure Interaction, Springer, 2006: pp. 371–385.

[43] S. Ali, C. Habchi, S. Menanteau, T. Lemenand, J.-L. Harion, Heat transfer and mixing enhancement by free elastic flaps oscillation, International Journal of Heat and Mass Transfer. 85 (2015) 250–264.

[44] R. Martin, R. Zenit, Heat Transfer Resulting From the Interaction of a Vortex Pair With a Heated Wall, Journal of Heat Transfer. 130 (2008) 051701.